MEMS Simulations and Waveguide Loss Analysis for Photonic Integrated Circuits

by

Berkin Binbas

Submitted to the Department of Physics
in partial fulfillment of the requirements for the degree of

BACHELOR OF SCIENCE IN PHYSICS

at the

MASSACHUSETTS INSTITUTE OF TECHNOLOGY

May 2024

Authored by: Berkin Binbas
Department of Physics
May 17, 2024

Certified by: Dirk Englund
Associate Professor of EECS, Thesis Supervisor

Accepted by: Lindley A. Winslow
Associate Professor of Physics
Associate Head, Department of Physics

MEMS Simulations and Waveguide Loss Analysis for Photonic Integrated Circuits

by

Berkin Binbas

Submitted to the Department of Physics
on May 17, 2024 in partial fulfillment of the requirements for the degree of

BACHELOR OF SCIENCE IN PHYSICS

ABSTRACT

Microelectromechanical systems (MEMS) are promising candidates to be used in photonic integrated chips (PICs) for applications. While there are a variety of MEMS devices used for different purposes, the main concern of this thesis will be the using MEMS as phase shifters and understanding waveguide losses. MEMS devices can be actuated by applying a potential difference, and can be used to adjust the phase shift of light travelling through the waveguides. The shift is observed as a result of the change of the physical distance between the cantilever and the fixed waveguides buried on the surface of the chips. Due to their ease of activation, ability to precisely control the phase shift, and small heat footprint, these devices are excellent candidates for cryogenic applications, such as quantum computers. In this work, we present a summary of the literature regarding the MEMS devices, and investigate their working principles. We introduce a simple theoretical model for understanding the two biggest source factors in characterization of MEMS devices: bending and propagation losses. We then present the experimental setup through used for performing loss measurements on a fabricated chip. We look at simulation results for understanding the behavior of the cantilever, perform loss analysis on measurements, and conclude with potential issues to be resolved for the devices to work as intended in the future.

Thesis supervisor: Dirk Englund
Title: Associate Professor of EECS

Acknowledgments

I would like to thank Mustafa Yucel, who has been my main day-to-day supervisor on the project, for helping me get started and make progress throughout all the steps of the project, and patiently answering all of my novice questions and providing me with resources to learn the subject. I would like to thank Carlos Errando Herranz for designing the chips, and providing guidance along the way as we learned more and more about the chips and the behavior of the devices. I would also like to thank Camille Papon and Alessandro Buzzi for all their efforts in the fabrication process of the chip. Lastly, I would like to thank Professor Englund for letting me join this project and use the equipment, overseeing the project and accepting to be my thesis supervisor.

Contents

List of Figures

List of Tables

Chapter 1

Overview and Organization

This thesis will be concerned with microelectromechanical systems (MEMS) devices in photonic integrated circuits (PICs) and understanding waveguide losses. In the path to scalable usage of MEMS as phase shifters in PICS, there are several problems that need to be resolved, one of which is understanding the losses of the fabricated chips. Thus, the main question we will try to answer in this thesis is how the intensity in a waveguide behaves as a function of the distance and bends it propagates through. We will attempt to explain the experimental observations with a simple exponential decay model using the least number of parameters possible at the end, in chapter 7.

The organization of the thesis is as follows: First, we will give a brief introduction to PICs and MEMS to motivate why one should study these and their importance for various applications, as well as why understanding the sources of on-chip losses is important in chapter 2. Then in chapter 3, we will study the background theory regarding light propagation in waveguides, some common photonic components that are tunable with MEMS, Kelvin polarization forces that enable the electrostatic actuation of MEMS and a simple model that lets us analyze two important sources of losses: bending and propagation losses. After that, we will introduce the MEMS, MZI and loss structure geometries that we worked with in chapter 4. Next, we will show some displacement simulations for the typical MEMS parameters in chapter 5, followed by the introduction of the experimental setup in chapter 6. Finally, we will perform loss analysis and evaluate our theoretical loss model in chapter 7, finishing off with the current problems and future directions in chapter 8.

Chapter 2

Introduction to PICs, MEMS and Waveguide Losses

In this chapter, we will closely follow the introduction given in [1] to PICs and MEMS. We will summarize the key points related to our topic. We first start by an overview of why PICs are important, followed by MEMS and their importance for realization of large scale PICs. We then proceed to explain 3 different ways PIC properties can be mechanically tuned. Lastly,

2.1 Why are PICs important?

PICs are chips that contain photonic components such as waveguides, phase shifters, and couplers. These are used to manipulate light, or photons, to achieve desired computational outcomes. They pose a faster low-power alternative to our traditional electronic computer chips that harness the power of semiconductors through transistors, resistors and capacitors. PICs are faster because all the computation is done through using light, as opposed to electrons in the classical electronic chips that are moving slower, and are more power efficient since there is no Joule heating. PICs are important for engineering applications, since they are able to achieve fast, low-power and low-cost computation through the usage of optical systems [1].

Most PIC platforms use Silicon as the main material for the waveguide. Silicon is chosen due to its large scale of high-quality manufacturability, CMOS compatibility, past experience with from the microelectronics industry and refractive index [1]. Applications of PICs range from high performance computing [2], which highlights that Silicon photonics will be able to achieve the required optical data communication bandwidths for fast computation, to quantum technologies [3], which emphasizes the potential of Silicon based PICs for providing physically guaranteed communications security and sub-shot-noise measurement [3].

As a result, the interest around scalable and easily manufacturable PIC technologies has increased over the last decade, leading to easy access to PIC prototyping [4], [5], which in turn lead to large-scale PIC implementations [1].

To be able to increase the scale which the PICs are manufactured and used, they need to be efficiently unable. Specifically, in order to reconfigure the PICs, or compensate for

	Power cons.	Optical loss	Foot-print	Speed	Limitations
Thermo-optic	--	++	+	+	Thermo-optic coefficient
Plasma dispersion	+	--	++	++	Semiconductors
Electro-optic (Pockels/Kerr)	++	+	--	++	Crystal symmetry
Opto-mechanic	--	+	+	+	Suspended and optical power dependent
MEMS	++	+	+	+	Suspended

++ Excellent + Medium – Limited

Table 2.1: Comparison of benefits and drawbacks of different tuning mechanisms for PICs. The figure is taken from [1]. Here, footprint refers to the propagation length.

variations in manufacturing and environmental perturbations, efficient tuning mechanisms of the waveguide properties are required.

Some common approaches to these tuning mechanism include using temperature dependence of the material that the waveguide is made from (which in turn changes the refractive index and thus the optical properties), plasma dispersion in semiconductors (which refers to the relation between the free carrier density in semiconductors and the complex refractive index [6]), Pockels or Kerr effects (which refers to the relation between the strong applied external electric field to a material and its change in refractive index [7]), displacement generated by optical gradient forces (optomechanics, which generates optical forces on the chip) and MEMS [1].

A qualitative comparison between the benefits and drawbacks of these different tuning mechanism can be seen in table 2.1 from [1]. The preferred mechanism depends on the application and the material used for PIC. For instance, Si has a large thermo-optic coefficent which makes it a good candidate for thermo-optic tuning, while SiN has a coefficient that is 10 times weaker and is not very suitable for the same method. For a more detailed discussion of the trade-offs between these mechanisms, please refer to [1]. The main outcome for us is that MEMS performs well enough for all the criteria of interest, while other methods lack in at least one criterion. This motivates a deeper look at MEMS.

The idea behind the usage of MEMS in PICs is to use mechanics at nano and micro scales and change the optical properties of waveguides, which we will now talk about in detail.

2.2 Why are MEMS important?

MEMS utilize mechanics at a nano to micrometer scale to introduce tuning of existing properties to compensate for fabrication variations and environmental perturbations in PICs, as well as adding new functionality. MEMS generally consist of a fixed component paired up with a movable component, and they are generally actuated by the application of a static electric field. Through the induced movement of the movable component, properties of the system that are dependent on the distance between the two components can be tuned as a function of the applied electric field. First batch-fabricated MEMS devices appeared in 1964 [8], and since then MEMS devices have been extensively used in different areas and products, such as accelerometers, gyroscopes and micromirror arrays [1].

As seen in table 2.1, MEMS have the benefit of very low power consumption and moderate amounts of optical loss on a PIC compared to other tuning mechanisms. Furthermore, some of these tuning properties do not work well with certain materials, but the working principle behind MEMS is agnostic to the material used [1]. Hence, MEMS is a plausible candidate that could help with scaling up the PIC manufacturing regardless of the material used.

2.2.1 Mechanical Tuning of PICs

We know briefly discuss the 3 main ways to mechanically alter the properties of waveguides in PICs. We will then focus on how MEMS can be used to realize one of these ways. The 3 ways are [1]:

- Applying compressive or tensile stresses to the waveguide to modify absorption and refractive index. Absorption modification could be used for tuning the power of the passing light, while changes in refractive index can be used for tuning the phase.
- Lengthening or shortening the waveguide segment along the propagation of direction. Again, this can be used to tune the power once loss per unit length is known. This also enables direct control of the phase, as a wave traveling on a longer path will accumulate a larger phase.
- Displacing a slab near the waveguide. This can be used to couple light into the slab and thus modify both the power and the phase, or just the phase.

For us, the third property will be of main concern. In what follows, we investigate how MEMS actuation can be used to displace a slab and tune various properties of light, most importantly the phase and the power within a given waveguide.

2.2.2 MEMS Tuning through Slab Displacement

For phase tuning, the general idea is that for light whose wavelength in vacuum is λ that is traveling in a waveguide of length L and effective refractive index n, the phase ϕ accumulated is

$$\phi = \frac{2\pi}{\lambda} nL$$

Hence, if n can be changed, the phase accumulated over a distance can be changed [1]. MEMS devices offer a way of displacing an external slab in the order of hundreds of nanometers through the actuation via an electric voltage, thereby changing n. Thus, MEMS devices can be used to build tunable phase shifters.

On the other hand, it could be the case that we wish to tune the power going through a given waveguide through mechanical displacement. One way to achieve this is to bring closer two waveguides that are capable of supporting the same mode (i.e. waveguides that have a very close effective refractive index). It can be shown that for two nearby slabs, the power ratio P_1/P_2 between the outputs is given by [1]:

$$\frac{P_1}{P_2} = \frac{\sin^2\left(\frac{\pi L \Delta n}{\lambda}\right)}{\cos^2\left(\frac{\pi L \Delta n}{\lambda}\right)}$$

where Δn is the difference between the effective refractive indexes of the two slabs, and L is the coupling length [1]. Thus, by using MEMS to change the physical distance between the two slabs and hence Δn, desired power output ratios can be achieved.

2.3 Why is understanding losses important?

We are interested in understanding the loss properties of the waveguides we are working with, because we would like to fabricate a low-loss PIC which is required for large, scalable systems. Otherwise, the input power has to be large enough to compensate for the losses on the chip, hence increasing the overall power consumption. Thus characterizing losses on a PIC are important for understanding how much of the input power is lost, which then lets us adjust the input power to match the desired power levels on the chip. These characterization also aid in fabricating chips with less and less loss as they give hints on what kinds of waveguides result in lower losses.

There have been extensive theoretical and numerical simulation studies of waveguide losses in the literature (for example, [9], [10]). The two most important sources of losses on PICs are bending and propagation losses.

In section 3.6, we will introduce a simple theoretical model for understanding these two major types of losses in waveguides. In section 7, we will assess the model with the measurements.

[1] We will consider the background theory of light propagation in waveguides and some related structures such as directional couplers later in section 3.

Chapter 3

Underlying Theory

In this chapter, we go through the related background theory for understanding the physics behind light propagation within waveguides, light coupling to the PICs for off-chip interfacing and working principles of MEMS.

3.1 Light Propagation in Waveguides

We begin by examining the properties of light propagation inside dielectric cavities known as waveguides. We will use Maxwell's equations, following [11] and [12], to derive the equations governing the propagation of the wave in a region of space filled with a material of linear dielectric constant ϵ. We will assume that the dielectric does not have magnetization, therefore $\mu = \mu_0$.

We begin with two of the Maxwell's equations.

$$\begin{cases} \nabla \times \mathbf{E} = -\frac{\partial \mathbf{B}}{\partial \mathbf{t}} \\ \nabla \times \mathbf{H} = \mathbf{J_f} + \frac{\partial \mathbf{D}}{\partial t} \end{cases}$$

Since we are inside a dielectric, there are no free currents, i.e. $\mathbf{J_f} = 0$. Furthermore, we can use the relations $\mathbf{D} = \epsilon \mathbf{E}$ and $\mathbf{B} = \mu_0 \mathbf{H}$ to write:

$$\begin{cases} \nabla \times \mathbf{E} = -\mu_0 \frac{\partial \mathbf{H}}{\partial t} \\ \nabla \times \mathbf{H} = \epsilon \frac{\partial \mathbf{E}}{\partial t} \end{cases} \tag{3.1}$$

Now, we assume that the waveguide is placed along the z axis. Thus, there is z symmetry in the system which means the amplitude of any vector field should not depend on z. Furthermore, we are interested in the non-static solutions to Maxwell's equations that result in waves travelling in the z direction. Hence, these solutions must take the form

$$\begin{cases} \mathbf{E} = \mathbf{E_0}(\mathbf{x},\ \mathbf{y}) e^{i(kz - wt)} \\ \mathbf{H} = \mathbf{H_0}(\mathbf{x},\ \mathbf{y}) e^{i(kz - wt)} \end{cases} \tag{3.2}$$

Let $\mathbf{E_0}(\mathbf{x},\ \mathbf{y}) = \mathbf{E_x}(\mathbf{x},\ \mathbf{y})\hat{\mathbf{x}} + \mathbf{E_y}(\mathbf{x},\ \mathbf{y})\hat{\mathbf{y}} + \mathbf{E_z}(\mathbf{x},\ \mathbf{y})\hat{\mathbf{z}}$ and plug $\mathbf{E}$ into eq. 3.1. The results we get for plugging in $\mathbf{H}$ will be identical with $\mathbf{E}$ and $\mathbf{H}$ swapped.

$$\nabla \times \mathbf{E} = \left(\frac{\partial}{\partial x}\hat{x} + \frac{\partial}{\partial y}\hat{y} + \frac{\partial}{\partial z}\hat{z}\right) \times \left(\mathbf{E_0}(\mathbf{x},\ \mathbf{y})e^{i(kz-wt)}\right) \tag{3.3}$$

$$= \left(\frac{\partial E_z}{\partial y}e^{i(kz-wt)} - \frac{\partial\left(E_y e^{i(kz-wt)}\right)}{\partial z}\right)\hat{x} + \left(\frac{\partial\left(E_x e^{i(kz-wt)}\right)}{\partial z} - \frac{\partial E_z}{\partial x}e^{i(kz-wt)}\right)\hat{y}$$

$$+ \left(\frac{\partial E_y}{\partial x}e^{i(kz-wt)} - \frac{\partial E_x}{\partial y}e^{i(kz-wt)}\right)\hat{z}$$

$$= \left(\frac{\partial E_z}{\partial y} - ikE_y\right)e^{i(kz-wt)}\hat{x} + \left(ikE_x - \frac{\partial E_z}{\partial x}\right)e^{i(kz-wt)}\hat{y}$$

$$+ \left(\frac{\partial E_y}{\partial x} - \frac{\partial E_x}{\partial y}\right)e^{i(kz-wt)}\hat{z}$$

$$= -\mu_0\frac{\partial\left(\mathbf{H_0}e^{i(kz-wt)}\right)}{\partial t} = -\mu_0\mathbf{H_0}(-iw)e^{i(kz-wt)}$$

$$\Rightarrow \begin{cases} \dfrac{\partial E_z}{\partial y} - ikE_y = iw\mu_0 H_x \\ ikE_x - \dfrac{\partial E_z}{\partial x} = iw\mu_0 H_y \\ \dfrac{\partial E_y}{\partial x} - \dfrac{\partial E_x}{\partial y} = iw\mu_0 H_z \end{cases}$$

Similarly, we can write the equations relating the components of $\mathbf{H}$ to $\mathbf{E}$ but with $\mu_0 \to -\epsilon$:

$$\begin{cases} \dfrac{\partial H_z}{\partial y} - ikH_y = -iw\epsilon E_x \\ ikH_x - \dfrac{\partial H_z}{\partial x} = -iw\epsilon E_y \\ \dfrac{\partial H_y}{\partial x} - \dfrac{\partial H_x}{\partial y} = -iw\epsilon E_z \end{cases} \tag{3.4}$$

From eqs. 3.3 and 3.4, we can find $E_x,\ E_y,\ H_x,\ H_y$ in terms of E_z and H_z. Starting from the middle eq. in 3.3, we can plug it into the top equation in 3.4:

$$iH_y = \frac{1}{w\mu_0}\left(ikE_x - \frac{\partial E_z}{\partial x}\right) \Rightarrow \frac{\partial H_z}{\partial y} - \frac{k}{w\mu_0}\left(ikE_x - \frac{\partial E_z}{\partial x}\right) - = -iw\epsilon E_x$$

$$\Rightarrow \boxed{i(k^2 - w^2\mu_0\epsilon)E_x = k\frac{\partial E_z}{\partial x} + w\mu_0\frac{\partial H_z}{\partial y}} \tag{3.5}$$

We can do the same for the top eq. in 3.3 and the middle eq. in 3.4:

$$iH_x = \frac{1}{w\mu_0}\left(\frac{\partial E_z}{\partial y} - ikE_y\right) \Rightarrow \frac{k}{w\mu_0}\left(\frac{\partial E_z}{\partial y} - ikE_y\right) - \frac{\partial H_z}{\partial x} = -iw\epsilon E_y$$

$$\Rightarrow \boxed{i(k^2 - w^2\mu_0\epsilon)E_y = k\frac{\partial E_z}{\partial y} - w\mu_0\frac{\partial H_z}{\partial x}} \tag{3.6}$$

Finally, we can do the same calculation the other way around to get H_x and H_y:

$$-iE_y = \frac{1}{w\epsilon}\left(ikH_x - \frac{\partial H_z}{\partial x}\right) \Rightarrow \frac{\partial E_z}{\partial y} + \frac{k}{w\epsilon}\left(ikH_x - \frac{\partial H_z}{\partial x}\right) = iw\mu_0 H_x$$

$$\Rightarrow \boxed{i(k^2 - w^2\mu_0\epsilon)H_x = k\frac{\partial H_z}{\partial x} - w\epsilon\frac{\partial E_z}{\partial y}} \tag{3.7}$$

$$-iE_x = \frac{1}{w\epsilon}\left(\frac{\partial H_z}{\partial y} - ikH_y\right) \Rightarrow -\frac{k}{w\epsilon}\left(\frac{\partial H_z}{\partial y} - ikH_y\right) - \frac{\partial E_z}{\partial x} = iw\mu_0 H_y$$

$$\Rightarrow \boxed{i(k^2 - w^2\mu_0\epsilon)H_y = k\frac{\partial H_z}{\partial y} + w\epsilon\frac{\partial E_z}{\partial x}} \tag{3.8}$$

Eqs. 3.5, 3.6, 3.7 and 3.8 can be used to compute all the wave vector components, once E_z and H_z are known. Thus, our next goal will be to find the equations governing E_z and H_z. We will assume a general $\epsilon = \epsilon(x,\ y)$, but still keep the assumption that the waveguide is symmetric along the z axis so that there is no z dependence. We now use the other two Maxwell's equations

$$\begin{cases} \nabla \cdot \mathbf{D} = \nabla \cdot (\epsilon \mathbf{E}) = 0 \Rightarrow (\nabla \epsilon) \cdot \mathbf{E} + \epsilon\,(\nabla \cdot \mathbf{E}) = 0 \\ \nabla \cdot \mathbf{H} = 0 \end{cases} \tag{3.9}$$

Noting the identity $\nabla \times (\nabla \times \mathbf{A}) = \nabla (\nabla \cdot \mathbf{A}) - \nabla^2 \mathbf{A}$ and using eq. 3.1, we get:

$$\nabla (\nabla \cdot \mathbf{H}) = \nabla \times (\nabla \times \mathbf{H}) + \nabla^2 \mathbf{H} = 0$$

$$\Rightarrow \nabla \times \left(\epsilon \frac{\partial \mathbf{E}}{\partial t} \right) + \nabla^2 \mathbf{H} = 0$$

Since $\frac{\partial \mathbf{E}}{\partial t} = -iw\mathbf{E}$, $\frac{\partial \mathbf{H}}{\partial t} = -iw\mathbf{H}$ and $\nabla \times (a\mathbf{A}) = a\nabla \times \mathbf{A} + (\nabla a) \times \mathbf{A}$, we get

$$(-iw\epsilon)\nabla \times \mathbf{E} - iw (\nabla \epsilon) \times \mathbf{E} + \nabla^2 \mathbf{H} = 0 \Rightarrow (iw\mu_0 \epsilon) \frac{\partial \mathbf{H}}{\partial t} - iw (\nabla \epsilon) \times \mathbf{E} + \nabla^2 \mathbf{H} = 0$$

$$\Rightarrow w^2 \mu_0 \epsilon \mathbf{H} - iw (\nabla \epsilon) \times \mathbf{E} + \nabla^2 \mathbf{H} = 0$$

$$\Rightarrow \boxed{\nabla^2 \mathbf{H} + w^2 \mu_0 \epsilon \mathbf{H} = -(\nabla \epsilon) \times \left(\frac{\nabla \times \mathbf{H}}{\epsilon} \right)} \tag{3.10}$$

We can derive a similar equation for the $\mathbf{E}$ field. Since $\nabla \cdot \mathbf{E} = -\frac{\nabla \epsilon}{\epsilon} \cdot \mathbf{E}$ from eq. 3.9, we have

$$\nabla (\nabla \cdot \mathbf{E}) = \nabla \times (\nabla \times \mathbf{E}) + \nabla^2 \mathbf{E} \Rightarrow \nabla \left(-\frac{\nabla \epsilon}{\epsilon} \cdot \mathbf{E} \right) = \nabla \times \left(-\mu_0 \frac{\partial \mathbf{H}}{\partial t} \right) + \nabla^2 \mathbf{E}$$

$$\Rightarrow -\nabla \left(\frac{\nabla \epsilon}{\epsilon} \cdot \mathbf{E} \right) = -\mu_0 \frac{\partial}{\partial t} (\nabla \times \mathbf{H}) + \nabla^2 \mathbf{E} = -\mu_0 \frac{\partial}{\partial t} \left(\epsilon \frac{\partial \mathbf{E}}{\partial t} \right) + \nabla^2 \mathbf{E} = w^2 \mu_0 \epsilon \mathbf{E} + \nabla^2 \mathbf{E}$$

$$\Rightarrow \boxed{\nabla^2 \mathbf{E} + w^2 \mu_0 \epsilon \mathbf{E} = -\nabla \left(\frac{\nabla \epsilon}{\epsilon} \cdot \mathbf{E} \right)} \tag{3.11}$$

Now, we make the simplifying assumption that $\epsilon(x,\ y) = \epsilon$ is a constant along the cross section of the dielectric. This is a realistic model for the waveguides that we are working with. In this case, the right hand side of eqs. 3.10 and 3.11 vanish. To get the equations for the z components, we multiply them both with $\hat{z}$ to get:

$$\boxed{\begin{cases} \dfrac{\partial^2 E_z}{\partial x^2} + \dfrac{\partial^2 E_z}{\partial y^2} + (w^2 \mu_0 \epsilon - k^2) E_z = 0 \\ \\ \dfrac{\partial^2 H_z}{\partial x^2} + \dfrac{\partial^2 H_z}{\partial y^2} + (w^2 \mu_0 \epsilon - k^2) H_z = 0 \end{cases}} \tag{3.12}$$

We see that E_z and H_z components obey the same equation, and the differences in the solution will be due to the boundary conditions.

3.2 Directional Couplers

We now look at one of the main components in our PICs, the directional couplers. We will follow a similar theoretical treatment given in chapters 2.1.1 and 2.1.2 of [13]. For a more detailed discussion, please refer to these chapters.

Directional couplers consist of two waveguides that are parallel and close to each other (please see figure 4.2) made from the same material. This enables the propagating waves within each waveguide to interact. As we will see, the length of the close by region, which we will call the coupling length, can be tuned to distribute power with desired ratios from one guide to the other. The relation between the coupled power and the overlapping length can be used to fabricate 50-50 directional couplers that split the power equally, which is used in the MZI that we will talk about in section 4.1.

We solve the wave propagation problem for such a system using what is called the "coupled-mode theory". For a detailed discussion, please refer to [14]. We begin by writing down the wave equation in a dielectric where speed of propagation is v:

$$\frac{\partial^2 \mathbf{E}}{\partial t^2} - v^2 \nabla^2 \mathbf{E} = 0 \tag{3.13}$$

We can use the fact that the traveling wave solutions satisfy the form $\mathbf{E}(\mathbf{r},\ t) = R(\mathbf{r})T(t)\hat{p}$, where $\hat{p}$ is the polarization direction of the field. We will assume that the polarization direction does not change, so we can write eq. 3.13 as a scalar equation for $E(\mathbf{r},\ t)$. Plugging this in above, we get:

$$R(\mathbf{r})\frac{d^2T(t)}{dt^2} - v^2 T(t)\nabla^2 \left(R(\mathbf{r})\right) = 0$$

$$\Rightarrow \frac{1}{R(\mathbf{r})}\nabla^2 R(\mathbf{r}) = \frac{1}{v^2 T(t)}\frac{d^2T(t)}{dt^2}$$

We notice that the left hand side is only a function of $\mathbf{r}$ and the right hand side is only a function of t. For them to be equal at all $\mathbf{r}$ and t values, we require them to be equal to some constant $-a^2$:

$$\frac{1}{R(\mathbf{r})}\nabla^2 R(\mathbf{r}) = \frac{1}{v^2 T(t)}\frac{d^2T(t)}{dt^2} = -a^2$$

Noting that $T(t) = e^{-iwt}$ (3.2), we have

$$-\frac{w^2}{v^2} = -a^2 \Rightarrow \frac{1}{R(\mathbf{r})}\nabla^2 R(\mathbf{r}) = -\frac{w^2}{v^2}$$

We note that $\frac{1}{v^2(x,\ y)} = \mu_0 \epsilon(x,\ y)$. If we now consider R to be not only a function of $\mathbf{r}$ but also w, we get the following equation for the spatial component of the electric field, which is known as the Helmholtz equation:

$$\nabla^2 R(\mathbf{r},\ w) + w^2\mu_0\epsilon(x,\ y)R(\mathbf{r},\ w) = 0 \tag{3.14}$$

Now, we introduce the base assumption of the coupled-mode theory: In the presence of two close waveguides made from the same material, the total field can be written as a superposition of the two fields within each waveguide, with the approximate following form:

$$\mathbf{R}(\mathbf{r},\ w) = R(\mathbf{r},\ w)\hat{p} \approx \left[B_1(x,\ y)A_1(z,\ w) + B_2(x,\ y)A_2(z,\ w)\right] e^{ikz}\hat{p} \tag{3.15}$$

where k is a constant. The intuition behind this solution is that $B_i(x,\ y)$ is the shape profile of the field when there is only one waveguide, and $A_i(z,\ w)$ is a term that regulates the amplitude of the field as a function of the coupling length and the frequency based on the interaction between the two waveguides. e^{ikz} is there for a traveling wave solution in the z direction.

We note that since $\hat{p}$ is assumed to be constant, the z component of each field is simply proportional to $R(\mathbf{r},\ w)$. As we have shown, $E_{zi}(x,\ y) = B_i(x,\ y)(\hat{p}\cdot\hat{z})$ for each field obeys eq. 3.12, thus we have

$$\frac{\partial^2 B_i}{\partial x^2} + \frac{\partial^2 B_i}{\partial y^2} + (w^2\mu_0\epsilon_i(x,\ y) - k_i^2)B_i = 0 \tag{3.16}$$

Here, we emphasize the fact that $\epsilon_i(x,\ y)$ is the dielectric constant distribution in space when only the ith waveguide is present. $\epsilon_i(x,\ y) = \epsilon_{iw}$ inside the ith waveguide, and $\epsilon_i(x,\ y) = \epsilon_0$ outside. We also note that $\epsilon_{1w} = \epsilon_{2w}$. Finally, $k_i^2 = \frac{w^2}{v_i^2} = w^2\mu_0\epsilon_{iw}$.

Now, to find the full approximate solution for $R(\mathbf{r},\ w)$, we need to determine $A_i(z,\ w)$'s as well. We first plug in eq. 3.15 to eq. 3.14 and discard $\hat{p}$:

$$\frac{\partial^2 B_1}{\partial x^2}A_1 e^{ikz} + \frac{\partial^2 B_1}{\partial y^2}A_1 e^{ikz} + B_1\frac{\partial^2 A_1 e^{ikz}}{\partial z^2} + \frac{\partial^2 B_2}{\partial x^2}A_2 e^{ikz} + \frac{\partial^2 B_2}{\partial y^2}A_2 e^{ikz} + B_2\frac{\partial^2 A_2 e^{ikz}}{\partial z^2}$$

$$+ w^2\mu_0\epsilon(x,\ y)\left[B_1A_1 + B_2A_2\right] e^{ikz} = 0 \tag{3.17}$$

We note that $\epsilon(x,\ y)$ in eq. 3.17 is the dielectric constant distribution in space when both of the waveguides are present at the same time, which is different from $\epsilon_i(x,\ y)$, which is the dielectric constant distribution in space when only one of the waveguides is present.

$$\frac{\partial^2 A_j e^{ikz}}{\partial z^2} = \frac{\partial}{\partial z}\left(\frac{\partial A_j}{\partial z}e^{ikz} + ikA_j e^{ikz}\right) = \left[\frac{\partial^2 A_j}{\partial z^2} + ik\frac{\partial A_j}{\partial z} + ik\left(\frac{\partial A_j}{\partial z} + ikA_j\right)\right] e^{ikz}$$

$$= \left[\frac{\partial^2 A_j}{\partial z^2} + 2ik\frac{\partial A_j}{\partial z} - k^2 A_j\right] e^{ikz}$$

Hence, eq. 3.17 can be written as

$$\left[\frac{\partial^2 B_1}{\partial x^2}+\frac{\partial^2 B_1}{\partial y^2}-k^2 B_1\right]A_1 e^{ikz}+\left[\frac{\partial^2 A_1}{\partial z^2}+2ik\frac{\partial A_1}{\partial z}\right]B_1 e^{ikz}$$

$$+\left[\frac{\partial^2 B_2}{\partial x^2}+\frac{\partial^2 B_2}{\partial y^2}-k^2 B_2\right]A_2 e^{ikz}+\left[\frac{\partial^2 A_2}{\partial z^2}+2ik\frac{\partial A_2}{\partial z}\right]B_2 e^{ikz}$$

$$+w^2\mu_0\epsilon(x,\ y)\left[B_1A_1+B_2A_2\right]e^{ikz}=0$$

Discarding e^{ikz} and using eq. 3.16, we can simplify this:

$$\left[\frac{\partial^2 A_1}{\partial z^2}+2ik\frac{\partial A_1}{\partial z}\right]B_1+\left(k_1^2-k^2+w^2\mu_0\left(\epsilon-\epsilon_1\right)\right)A_1B_1$$

$$+\left[\frac{\partial^2 A_2}{\partial z^2}+2ik\frac{\partial A_2}{\partial z}\right]B_2+\left(k_2^2-k^2+w^2\mu_0\left(\epsilon-\epsilon_2\right)\right)A_2B_2=0$$

Finally, we multiply this with B_1^* and B_2^* to get the following two equations:

$$A_1|B_1|^2\left(k_1^2-k^2+w^2\mu_0\left(\epsilon-\epsilon_1\right)\right)+A_2B_1^*B_2\left(k_2^2-k^2+w^2\mu_0\left(\epsilon-\epsilon_2\right)\right)+$$
$$|B_1|^2\left[\frac{\partial^2 A_1}{\partial z^2}+2ik\frac{\partial A_1}{\partial z}\right]+B_1^*B_2\left[\frac{\partial^2 A_2}{\partial z^2}+2ik\frac{\partial A_2}{\partial z}\right]=0$$

$$A_1B_1B_2^*\left(k_1^2-k^2+w^2\mu_0\left(\epsilon-\epsilon_1\right)\right)+A_2|B_2|^2\left(k_2^2-k^2+w^2\mu_0\left(\epsilon-\epsilon_2\right)\right)+$$
$$B_1B_2^*\left[\frac{\partial^2 A_1}{\partial z^2}+2ik\frac{\partial A_1}{\partial z}\right]+|B_2|^2\left[\frac{\partial^2 A_2}{\partial z^2}+2ik\frac{\partial A_2}{\partial z}\right]=0$$

Now, we integrate over the $x-y$ plane. We will do this explicitly for B_1^* to see what form of an equation we obtain, and use the result to derive the equation for B_2^*. We will use the normalization $\int\int|B_i|^2dxdy=1$.

$$A_1\left(k_1^2-k^2\right)+A_1w^2\mu_0\int|B_1|^2(\epsilon-\epsilon_1)dxdy+A_2\left(k_2^2-k^2\right)\int B_1^*B_2dxdy$$
$$+A_2w^2\mu_0\int B_1^*B_2(\epsilon-\epsilon_2)dxdy+\left[\frac{\partial^2 A_1}{\partial z^2}+2ik\frac{\partial A_1}{\partial z}\right]+\left[\frac{\partial^2 A_2}{\partial z^2}+2ik\frac{\partial A_2}{\partial z}\right]\int B_1^*B_2dxdy=0$$

Finally, we are ready to make some approximations to this equation to simplify the complexity. First of all, we will assume that the single waveguide solutions B_i are small outside of the waveguide, hence we will take $\int B_i^*B_jdxdy\approx 0$. We also note that $\epsilon-\epsilon_i=0$

everywhere except at the location of the other waveguide, therefore $\int |F_1|^2(\epsilon - \epsilon_1)dxdy \approx 0$ as well, due to the small field assumption. We note that we will keep the term $\kappa_{12} \equiv \int F_1^* F_2(\epsilon - \epsilon_2)dxdy$ that multiplies A_2 as a first order approximation to the coupling between the waveguides, i.e it is the "leading term" of all the terms that we approximated to zero. All these approximations result in the following simplified equation:

$$\left[\frac{\partial^2 A_1}{\partial z^2} + 2ik\frac{\partial A_1}{\partial z}\right] = -A_1(k_1^2 - k^2) - 2kA_2\kappa_{12}$$

If we assume the two waveguides are fully symmetric, then we should have $k_1 = k_2 = k$. And as a final step, to make the final equations even easier to work with, we will assume the second z derivative of A_i is small compared to the first z derivative term. Thus, we obtain the following two equations (after going through the same steps with B_2^*):

$$\begin{cases} \dfrac{\partial A_1}{\partial z} = i\kappa A_2 \\ \dfrac{\partial A_2}{\partial z} = i\kappa A_1 \end{cases}$$

where $\kappa = \kappa_{12} = \kappa_{21}$ due to symmetry. Taking a derivative of the first eq. and using the second eq., we get

$$\frac{\partial^2 A_1}{\partial^2 z} = -\kappa^2 A_1 \Rightarrow \begin{cases} A_1 = A\cos(\kappa z) + B\sin(\kappa z) \\ A_2 = \dfrac{1}{i\kappa}\dfrac{\partial A_1}{\partial z} = -i(-A\sin(\kappa z) + B\cos(\kappa z)) \end{cases}$$

If there is input power only at waveguide 1, we have $A_1(0) = A_0,\ A_2(0) = 0 \Rightarrow A = A_0,\ B = 0$. Thus

$$\frac{\partial^2 A_1}{\partial^2 z} = -\kappa^2 A_1 \Rightarrow \begin{cases} A_1 = A_0\cos(\kappa z) \\ A_2 = -iA_0\sin(\kappa z) \end{cases}$$

As the power carried is proportional to the field amplitude squared, letting $P_0 = |A_0|^2$, we get the following equation for directional couplers:

$$\begin{cases} P_1 = P_0\left(\cos(\kappa z)\right)^2 \\ P_2 = P_0\left(\sin(\kappa z)\right)^2 \end{cases} \tag{3.18}$$

Eq. 3.18 is the power coupling equation for a lossless, symmetric directional coupler. It is striking that through modulation of the coupling distance z, the power transmitted from one waveguide to the other can be adjusted. The coupling lenghts in our chips are adjusted such that there is a 50:50 division of power.

3.3 Phase Shifters

The main functionality that we want to achieve with MEMS is tunable phase shifting. Here, we look at the phase shift as a function of the effective refractive index.

As was mentioned in section 2.2.2, for any light propagating a distance L through a medium with refractive index n, and vacuum wavelength λ, the phase accumulated can be written as

$$\phi = \frac{2\pi}{\lambda} nL$$

As will be evident from the MEMS geometries we are working with in section 4.2, we have a fixed L. Therefore any change in the phase can be induced through changing the effective refractive index of the medium:

$$\Delta\phi = \frac{2\pi}{\lambda} \Delta nL$$

We would like to cover the whole range of 0 to 2π phase shifts with our MEMS phase shifters. For the two wavelengths $\lambda_1 = 620\,\text{nm}$ and $\lambda_2 = 737\,\text{nm}$ the chips were designed for and a typical cantilever length of $L = 40\,\mu\text{m}$ (please see figure 4.1), we can calculate the required effective refractive index change to cover this whole range:

$$2\pi = \frac{2\pi}{\lambda}\Delta nL \Rightarrow \Delta n = \frac{\lambda}{L} \Rightarrow \begin{cases} \Delta n_1 \approx 0.016 \\ \Delta n_2 \approx 0.018 \end{cases}$$

According to simulations results in [15], a displacement of 50 nm is capable of achieving a refractive index change of $\sim 0.06 - 0.07$ for the given wavelengths. Thus, as long as the designed MEMS can achieve a displacement in the order of 50 nm, we should be able to tune the full phase shift range.

3.4 Kelvin Polarization Forces for MEMS Actuation

Lastly, we need to know how much voltage needs to be applied in order to displace the cantilever to change the refractive index and hence cause a desired phase shift. In this section, we introduce the mechanism behind the cantilever displacement, the Kelvin polarization forces. We will follow the explanations and derivation in [16] closely. To see diagrams of the actual MEMS geometries, please refer to figures 4.1 and 4.3.

Kelvin polarization forces occur due to inhomogeneous electric fields applied to dielectric materials. The field gradient causes different parts of the dielectric to polarize differently, and causes a non-homogeneous force per unit volume:

$$\mathbf{f} = \mathbf{P} \cdot (\nabla \mathbf{E}) \tag{3.19}$$

where $\mathbf{P} = \frac{\mathbf{dp}}{dV}$ is the dipole moment per unit volume, and $\mathbf{E}$ is the external electric field. As evident from eq. 3.19, a nonhomogeneous electric field is essential for the force density to be nonzero.

Using this fundamental relation, we can understand what happens when a dielectric beam is placed over the gap between two coplanar electrodes. Due to the inhomogeneous field, the polarized beam will feel a force, and depending on the relative permittivities of the material and the environment, the beam will be either attracted towards the gap or repelled away.

For linear dielectrics, we have

$$\mathbf{P} = \epsilon_0 \chi \mathbf{E} = \epsilon_0(\epsilon_r - 1)\mathbf{E}$$

where ϵ_r is the relative permittivity of the material. Thus eq. 3.19 can be rewritten as

$$\mathbf{f} = \frac{1}{2}\epsilon_0(\epsilon_r - 1)\nabla(\mathbf{E}\cdot\mathbf{E}) \tag{3.20}$$

If the dielectric is embedded in a medium of permittivity ϵ_m, then eq. 3.20 can be written as

$$\mathbf{f} = \frac{1}{2}\epsilon_0(\epsilon_r - \epsilon_m)\nabla(\mathbf{E}\cdot\mathbf{E})$$

Intuitively, this can be thought of as the polarization of the external medium weakening the overall external field "felt" by the embedded material, as the medium's polarization will create a field opposite to the external field. Consequently, the total Kelvin polarization force over the entire volume V of the dielectric material can be written as

$$\mathbf{F} = \int_V \frac{1}{2}\epsilon_0(\epsilon_r - \epsilon_m)\nabla(\mathbf{E}\cdot\mathbf{E})dV \tag{3.21}$$

Now, for two very thin coplanar electrodes that have a very small gap between them, it is known that the electric field can be approximated to have radial symmetry, with the origin of symmetry located at the midpoint between the plates. For an applied voltage U, E is given by

$$E_{ext} = \frac{U}{\pi r}$$

where r is the radial distance from the origin. However, this equation is only valid when ϵ_m and ϵ_r are equal to each other, as it is assumed that there are no distortions to the electric field by the medium. In reality, there will be perturbations to this cocentric electric field due to the induced field of the dielectric. In order to account for these perturbations and the change of the electric field inside the dielectric, we introduce a factor α:

$$E_r = \alpha E_{ext}$$

where E_r is the strength of the electric field inside the dielectric. Now, let's assume that the cocentric electric fields are on the $x-y$ plane. Assume that the cantilever of the MEMS is suspended along the y axis, and we are interested in finding the forces that cause a displacement in this axis, as shown in figure 4.3. Thus, using eq. 3.21, we can write the total y component of the Kelvin polarization force acting on this dielectric:

$$F_y = \int_0^L \int_{-w/2}^{w/2} \int_{y-h/2}^{y+h/2} \frac{1}{2}\epsilon_0(\epsilon_r - \epsilon_m)\frac{\partial(\mathbf{E}\cdot\mathbf{E})}{\partial y} dz dx dy$$

$$= \frac{L}{2}\epsilon_0(\epsilon_r - \epsilon_m)\int_{-w/2}^{w/2} \int_{y-h/2}^{y+h/2} \frac{\partial(\mathbf{E}\cdot\mathbf{E})}{\partial y} dx dy$$

where L is the overlapping length of the waveguides. Let's first calculate the partial derivative of the field:

$$\frac{\partial\left(\mathbf{E}\cdot\mathbf{E}\right)}{\partial y}=\alpha^2\frac{U^2}{\pi^2}\frac{\partial}{\partial y}\left(\frac{1}{x^2+y^2}\right)=\alpha^2\frac{-2yU^2}{\pi^2(x^2+y^2)^2}$$

$$\Rightarrow F_y=-\alpha^2\frac{LU^2}{\pi^2}\epsilon_0(\epsilon_r-\epsilon_m)\int_{-w/2}^{w/2}\int_{y-h/2}^{y+h/2}\frac{y}{(x^2+y^2)^2}dxdy$$

Let's calculate the integral:

$$I=\int_{-w/2}^{w/2}\int_{y-h/2}^{y+h/2}\frac{y}{(x^2+y^2)^2}dxdy=-\frac{1}{2}\int_{-w/2}^{w/2}\frac{1}{x^2+y^2}dx\Bigg|_{y-h/2}^{y+h/2}$$

$$=\frac{1}{2}\int_{-w/2}^{w/2}\left(\frac{1}{x^2+(y-h/2)^2}-\frac{1}{x^2+(y+h/2)^2}\right)dx$$

Let's calculate one of these integrals:

$$I_u=\int\frac{dx}{x^2+u^2}=\frac{1}{u}\int\frac{d\phi}{1+\phi^2}=\frac{1}{u}\int\frac{\sec^2(\theta)d\theta}{\sec^2(\theta)}=\frac{1}{u}\arctan\left(\frac{x}{u}\right)$$

$$\Rightarrow I=\frac{\arctan\left(\frac{w}{2(y-h/2)}\right)}{y-h/2}-\frac{\arctan\left(\frac{w}{2(y+h/2)}\right)}{y+h/2}$$

$$F_y=\alpha^2\frac{LU^2}{\pi^2}\epsilon_0(\epsilon_r-\epsilon_m)\left(\frac{\arctan\left(\frac{w}{2(y+h/2)}\right)}{y+h/2}-\frac{\arctan\left(\frac{w}{2(y-h/2)}\right)}{y-h/2}\right)<0$$

Here, we note that as long as $\epsilon_r-\epsilon_m>0$ (which is the case for SiN and air, since $\epsilon_r\approx 8$ and $\epsilon_m\approx 1$), this force is attractive towards the plates, as desired. Now, we model the MEMS cantilever as a spring with some effective spring constant k. Let's assume that the initial vertical distance from the electrode plane to the center of the cantilever is y_0. This already includes the displacement of equilibrium position due to gravity. Thus, the vertical spring force pulling the cantilever back will be

$$F_{spring,\ y}=k(y_0-y)>0$$

since $y<y_0$ (cantilever has descended). Combining this with eq. 3.4, we get

$$F_y + F_{spring,\ y} = 0$$

$$\Rightarrow \boxed{k(y_0 - y) = \alpha^2 \frac{LU^2}{\pi^2} \epsilon_0 (\epsilon_r - \epsilon_m) \left(\frac{\arctan\left(\frac{w}{2(y-h/2)}\right)}{y - h/2} - \frac{\arctan\left(\frac{w}{2(y+h/2)}\right)}{y + h/2} \right)} \tag{3.22}$$

Eq. 3.22 will be used in chapter 5 to plot the vertical displacement of the cantilever as a function of the applied potential for different k values as well as the experimental value.

3.5 Grating Couplers for Off-chip Interface

We now briefly introduce grating couplers due to being part of the on-chip MZI structure for enabling off-chip interfacing.

These structures, as schematically shown in figure 3.1, allow the incoming light from the fiber array above the chip to be coupled into the waveguides on the surface of the chip. When the light reaches to one of these at the other end of the waveguide, this time the grating couplers serve the purpose of sending the light out of chip's plane, back into the fibers.

The incidence angle of light from the fibers has to be adjusted according to the wavelength used. The angle to achieve maximum in-plane coupling can be determined from the following grating equation [17]:

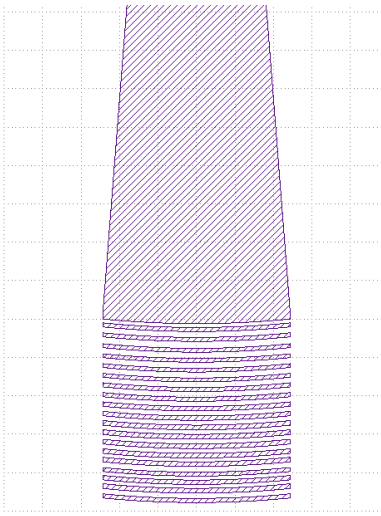

Figure 3.1: A zoomed-in image of the grating couplers from the GDS file. The grating spacing $\Lambda = 0.3\,\mu\text{m}$.

$$k_0 \sin(\theta) + mG = \beta_m$$

where $k_0 = \frac{2\pi}{\lambda_0}$ is the wave vector in of the incident light in the air, θ is the angle between the vertical and the incident light direction, m is the diffraction order, $G = \frac{2\pi}{\Lambda}$ is the grating

vector, and $\beta_m = \frac{2\pi n_{eff}}{\lambda_0}$ is the wave vector of the coupled light in the chip. Here, Λ is the grating spacing.

For us, $\lambda_0 = 620\,\text{nm}$, $\Lambda = 0.3\,\mu\text{m}$, $n_{eff} \approx 1.75$. Putting all these in, we see that the highest diffraction order that couples onto the chip is $m = 1$ with $\theta \approx 18°$. So this was the tilt angle used for the fibre array for all the measurements.

Due to the symmetry, when the light encounters the same structure at the other end of the waveguide, it leaves the chip with the same incidence angle. Thus, it can be efficiently sent and collected by a single fiber array tilted to the incidence angle.

3.6 Theoretical Model for Waveguide Loss Analysis

Finally, we introduce a theoretical model for waveguide loss analysis for comparison with measurements.

Propagation losses occur at sections where the waveguide is straight, due to absorption and non-perfect confinement of the traveling wave. On the other hand, bending losses occur at sections where the waveguide bends, due to the mismatch between the modes of the straight waveguide and the bent waveguide and scattering losses [15]. So on a bent section, in addition to the usual propagation losses, there are additional losses. In general, the higher the radius of curvature is, the more the bending loss should be. However, in our measured structures, the radii of curvature of bends were within the range $10\,\mu\text{m} - 12\,\mu\text{m}$, therefore in our theoretical model we neglected the variation of the bending loss coefficient in this small range.

We now introduce the theoretical model for waveguide losses. We will assume an exponential decay as a function of the distance traveled within the waveguide. One of the reasons why an exponential decay is chosen as the basis of the model is that it is a nice, well-behaved function that can be used to approximate linear, quadratic, etc. functions with proper coefficients in the exponents (i.e. if the coefficient is very close to one, on small distances compared to the coefficient, the exponential function approximates a linear function). Another reason is that we would like to describe the observed losses with a relatively simple model with few parameters. With this assumption, we will define two constants α and β as the propagation and bending loss per unit distance, respectively:

$$\begin{cases} I_{prop}(z) = I_0 e^{-\alpha z} \\ I_{bend}(z) = I_0 e^{-\beta z} \end{cases} \tag{3.23}$$

where z is the distance travelled either in a straight or a bent waveguide. As we will see when discussing measurement results in section 7, while being far from perfect, this model is especially accurate when modeling the losses in waveguides that are dominated by bends, while it is not so useful for waveguides dominated by straight sections.

When reporting measurement results, we will report the so-called dB loss:

$$\text{dB loss} = 10 \log_{10} \frac{\text{Measured intensity}}{\text{Reference intensity}} \tag{3.24}$$

With the exponential loss model of eq. 3.23, we expect that number of bends vs. dB loss is a line, as well as length of spiral waveguide vs dB loss.

Chapter 4

MEMS, MZI and Loss Structure Geometry

In this chapter, we will describe the MEMS, MZI and loss struscture geometries that we have worked with. We note that the waveguides are made of SiN, while the etched substrate of the chip is made from SiO_2.

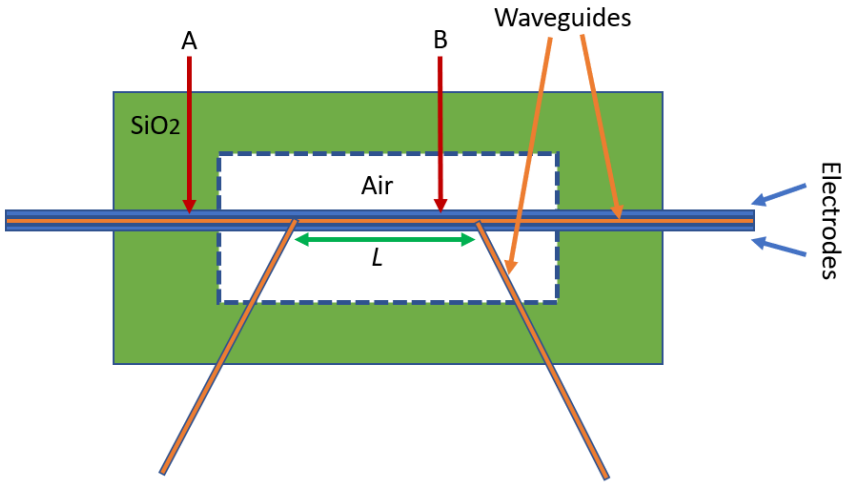

Figure 4.1: Top view of a MEMS. The SiO_2 in the dashed white rectangular region is etched, thus revealing the cantilever suspended in the air. SiN waveguides are labeled in orange, electrodes in blue. Points A and B are the cross section points in figure 4.3. L is the overlapping length between the cantilever and the fixed waveguide. Figure redrawn from [15].

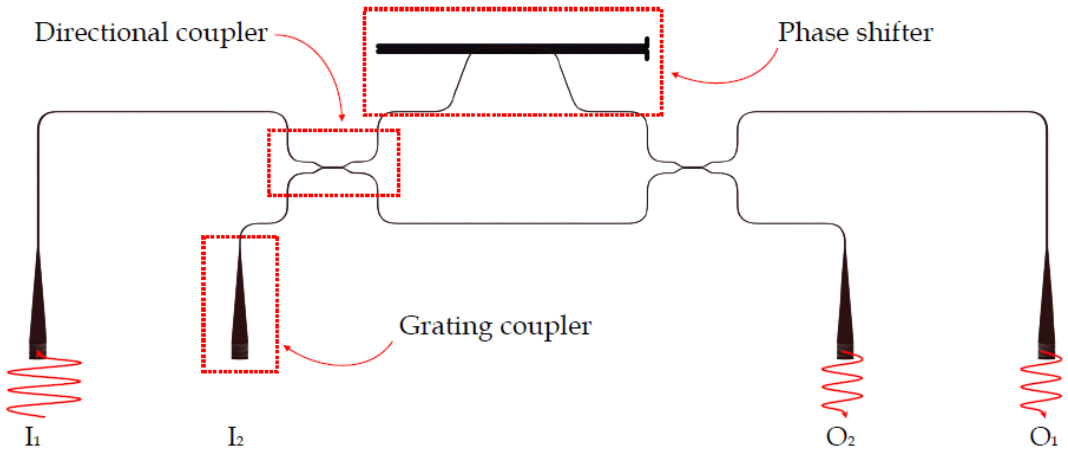

Figure 4.2: A diagram for a typical MZI found on our chips. The MZI consists of input grating couplers to couple the light from the off-chip fiber arrays into the on-chip waveguides, directional couplers to split the light into two 50-50 waves, a MEMS phase shifter, and output grating couplers to couple the light back into the fiber array for transmission to the spectrometer. Figure taken from [15].

4.1 Typical Mach-Zehnder Interferometer (MZI) Geometry

After fabrication of a MEMS device, one way to check whether the waveguides are intact and are guiding the light as intended is to look at its output without actuation. The output should resemble that of what is called the MZI, which is an interferometer used for sensing small changes in system parameters such as path length and effective refractive index. This interferometer is constructed by first splitting an input beam into two beams with equal intensities using a directional coupler, then these two beams travel in different arms before recombining through another directional coupler. The resulting recombined beam intensity as a function of the wavelength is used to determine the relative optical path differences of the two arms. If the wavelength-intensity measurements shift, then it means that the optical path difference between the two arms has changed. This underlying idea of an MZI can be used for observing the phase shifts due to MEMS actuation, since actuation changes effective refractive index on one of the arms, therefore changing the relative optical path difference between the two arms. We show a diagram of a typical MZI in our chips in figure 4.2.

4.2 Typical MEMS Geometry

We show the cross section along the wave propagation direction of a typical MEMS geometry that we have worked with.

In figure 4.1, a schematic of the top view of MEMS can be seen. In figure 4.3, the cross section along the propagation direction can be seen.

In figure 4.4, an array of actual MEMS devices that we have been working with can be

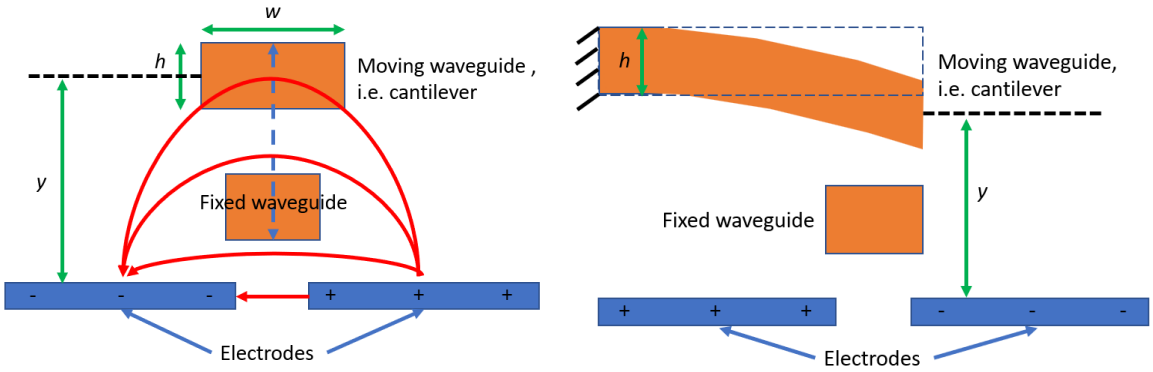

Figure 4.3: Two cross sections showing the MEMS as seen from the two points A and B in figure 4.1. The left figure is from point A and the right figure from point B. In the left figure, the blue rectangles at the bottom are the electrodes with the red electric field lines going from the higher potential plate (+) to the lower potential plate (-). The orange rectangles are the waveguides, with the bottom waveguide being the fixed and the top waveguide being the moving one. As a result of the Kelvin polarization forces, the top waveguide can be displaced along the vertical dashed blue line. Some useful parameters for force calculation are also labeled: w - width and h - height of the moving waveguide, and y - the initial height of the midpoint from the electrodes. In the right figure, the bending of the cantilever can be seen. Figures redrawn from [15].

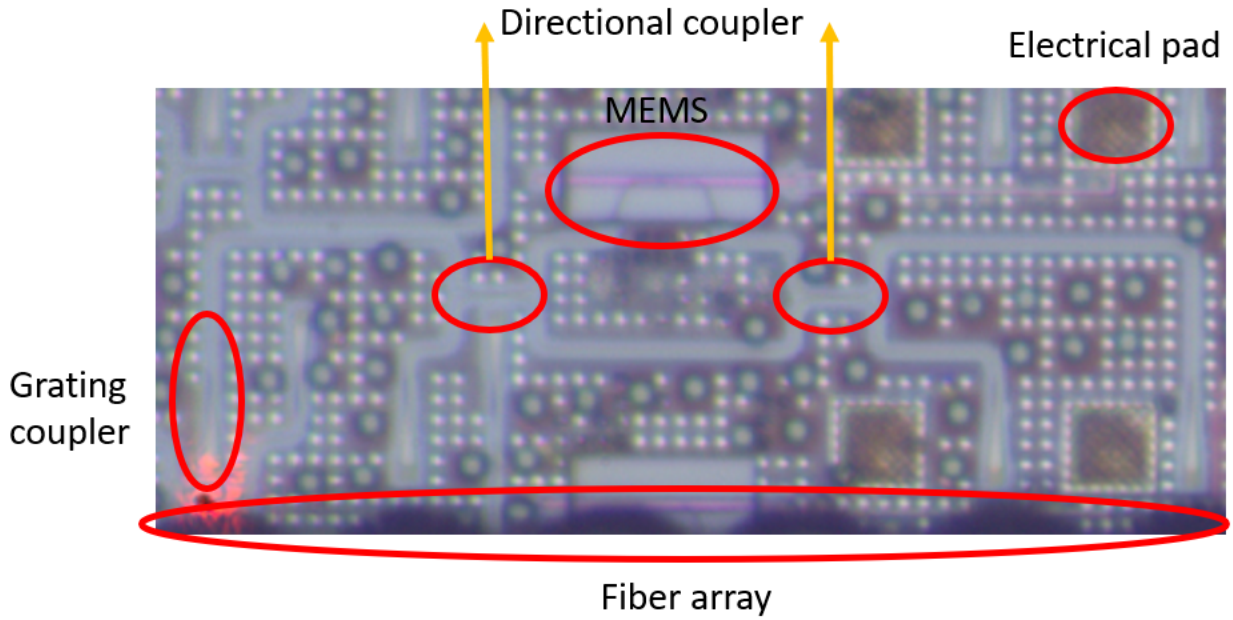

Figure 4.4: An array of actual MEMS devices under camera. Various other structures of interest, such as the electrical pads, grating couplers, directional couplers and the fiber array have also been highlighted. The laser from the fiber array at the bottom left corner can also be seen.

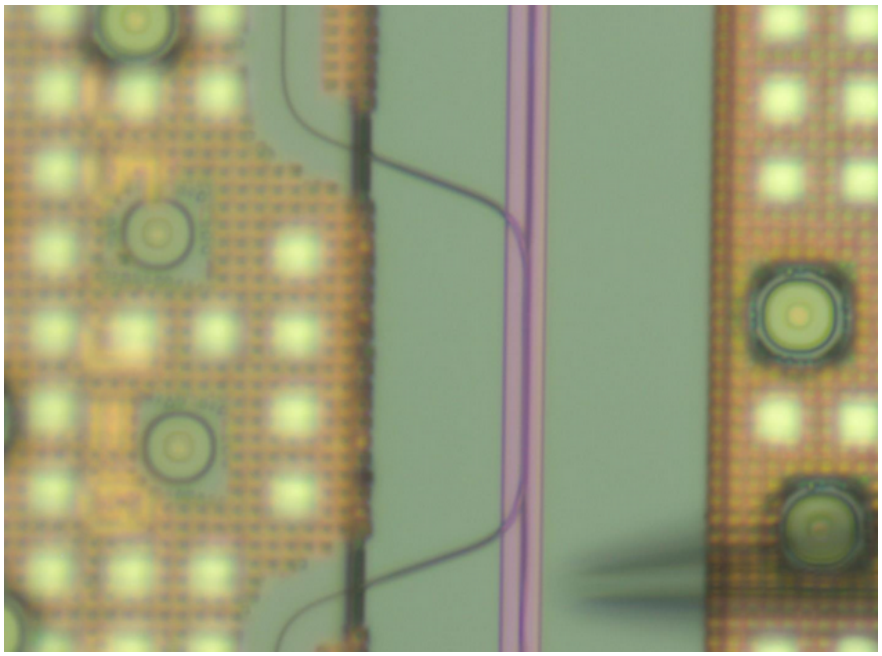

Figure 4.5: A closer image of an actual MEMS under light microscope. The pink plates below are the plates of the capacitor that generate the electric field, while the black vertical line that goes between them is the fixed waveguide. The movable waveguide, i.e. the cantilever that is similar to a widened “U" shape can be seen to be on top of the fixed waveguide.

seen. Other highlighted structures in the figure include electrical pads for applying voltage to the capacitor plates and directional couplers.

And in figure 4.5, a close-up image can be seen. Most of the devices that were designed, manufactured and tested were of similar geometry, with slight variations in the cantilever length and curvatures around the edges.

Lastly in figure 4.6, an SEM image of a MEMS can be seen, along with the suspended and “stuck" sections.

In figures 4.7, we can see the bending and spiral waveguides that will be used for loss analysis in chapter 7, respectively.

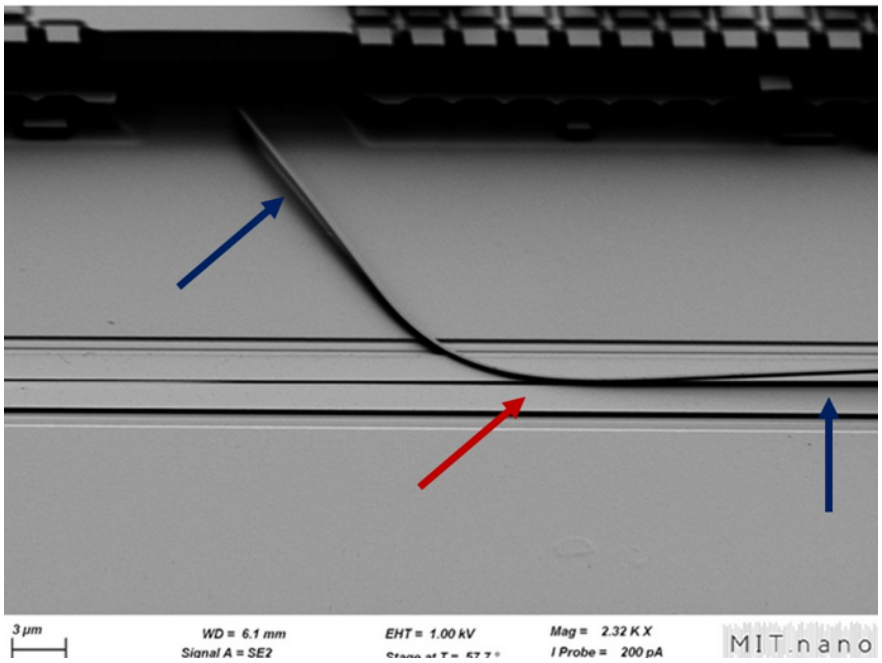

Figure 4.6: SEM image of a MEMS device. One prevalent issue that we will elaborate more on under section 8 is that as seen in this figure, the lower left corner of the cantilever (shown with a red arrow) is stuck to the substrate below. However, the top left and lower right portions pointed by the blue arrows can be seen to be suspended. This “stiction" prevents the actuation of device with electric field. The image was taken at MIT Nano.

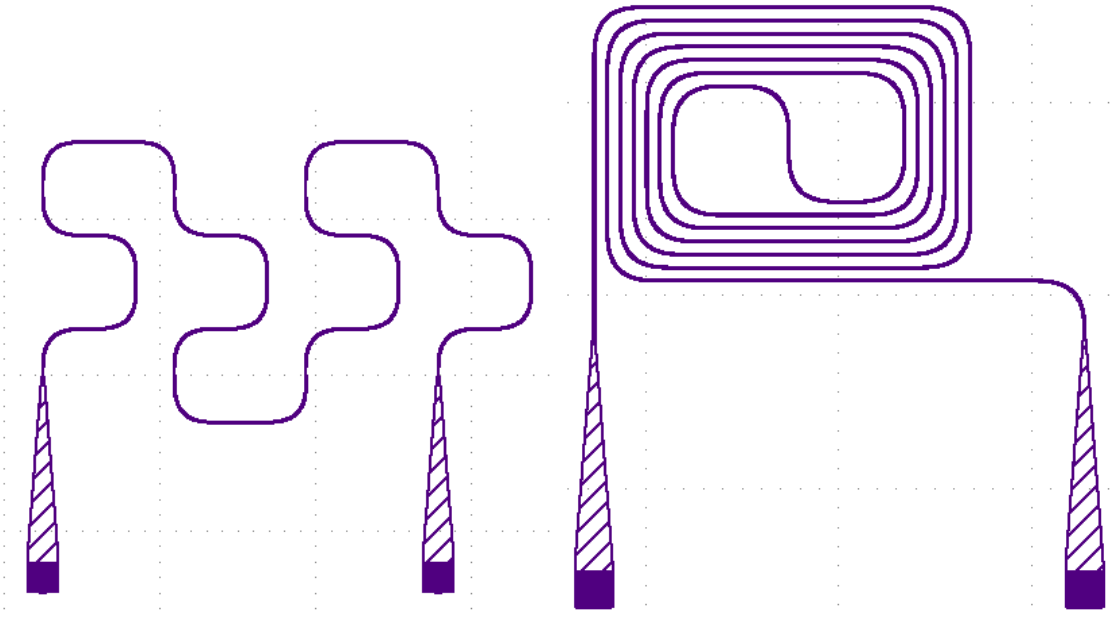

Figure 4.7: Typical bending and spiral waveguides for bending and propagation loss measurements is shown, left to right.

Chapter 5

Displacement Simulations

In this chapter, we share numerical results for the MEMS cantilever displacement as a function of the electric voltage applied to the capacitor. We also share the numerically calculated spring constant value from which we get an order of magnitude estimation for what the voltage should be for observing cantilever displacements that would result in a 2π phase shift.

First, we graph the displacement of the cantilever as a function of the voltage, assuming eq. 3.22, for different values of k. We used the typical values of $h = 220\,\text{nm}$, $w = 2h = 440\,\text{nm}$, $L = 40\,\mu\text{m}$, $y_0 = 420\,\text{nm}$ for the MEMS geometry, and $\epsilon_0 = 8.854 \times 10^{-12} F/m$, $\epsilon_r = 8$, $e_m = 1$ (air), and $a = 0.7$ (obtained from the simulations made in [16]). The results can be seen in figure 5.1a.

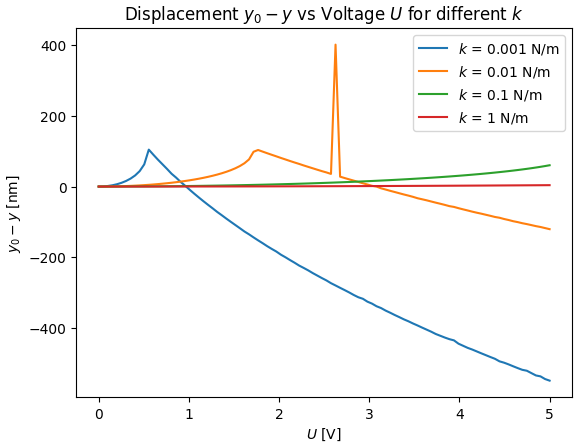

(a) Vertical displacement as a function of U for different k values. As the spring gets stiffer, i.e. k increases, more voltage is needed to achieve the same displacement. There seems to be a numerical instability for $k = 0.01\ N/m$ around 2.8 volts.

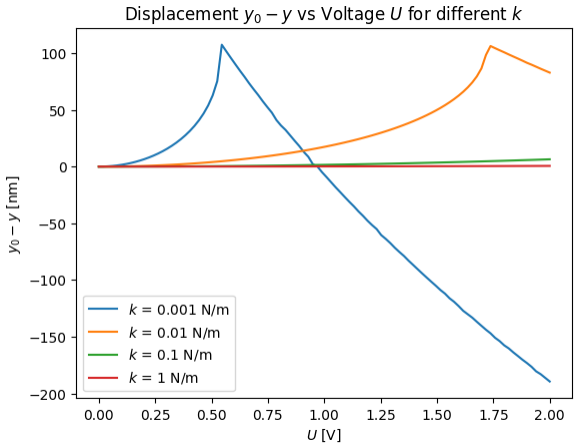

(b) Zoomed in version of the figure on the left. As we see, the maximum displacement is around 100 nm, which is more than enough for a 2π phase shift according to section 3.3.

In order to understand the exact displacement response as a function of the applied potential, we need to know the numerical value for k (see eq. 3.22). We have used COMSOL

[18] for extracting the value of k:

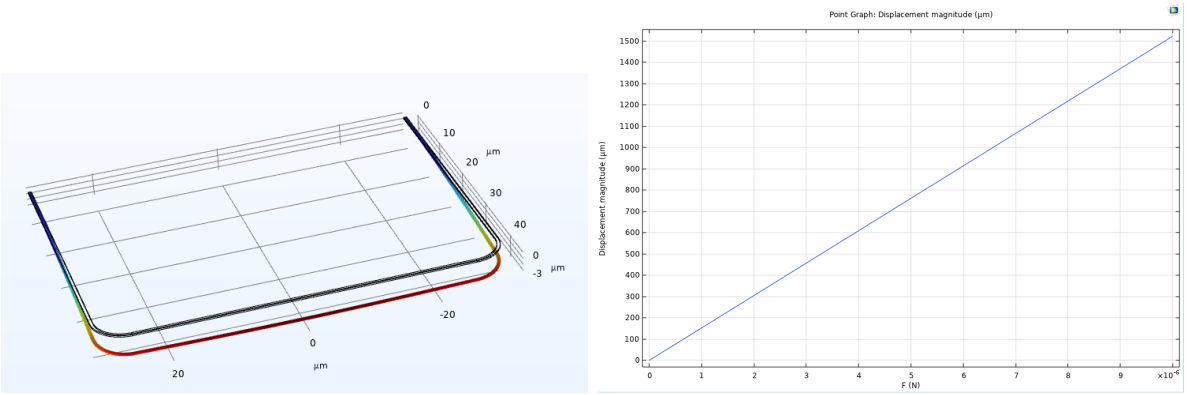

Figure 5.2: COMSOL simulations for a typical MEMS cantilever. A 3-D rendering of the displaced waveguide under force can be seen on the left, and the force vs. displacement graph can be seen on the right.

From the figure 5.2, we see that $k \approx 6.6 \times 10^{-3}\ N/m$. Thus, the theoretical voltage vs. displacement curve has been redrawn with this value of k on figure 5.3. As seen, a maximum displacement of around 100 nm can be achieved around 1.4 V. This sets the order of magnitude for the voltage values that we expect to apply to the system for a 2π phase shift.

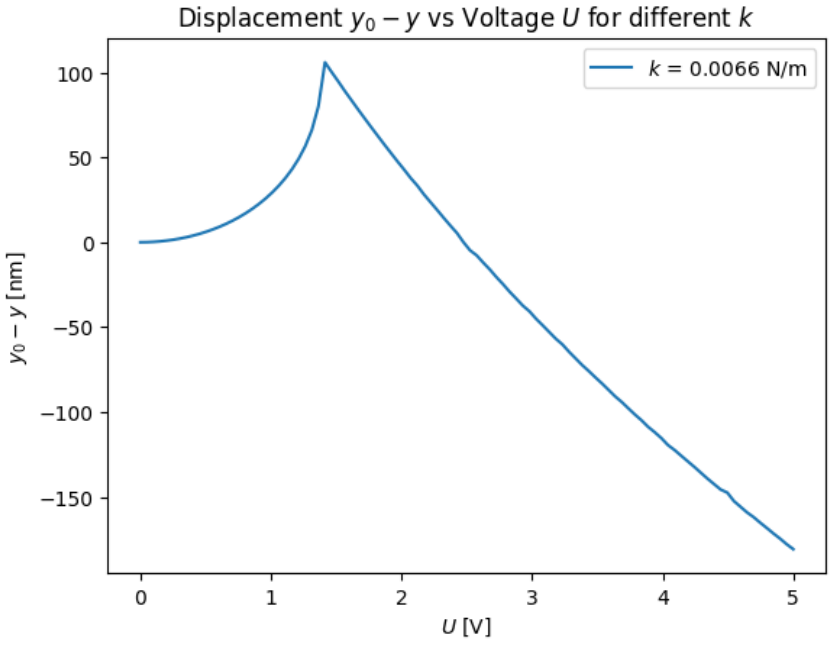

Figure 5.3: Numerical simulations of eq. 3.22 for $k = 6.6 \times 10^{-3}\ N/m$.

Chapter 6

Experimental Setup

In this chapter, we present the experimental setup used for measurements in chapter 7. We will give a physical overview of the setup as well as that of the codebase, which was used for writing a GUI for interacting with various instrumentation and automation of some processes.

6.1 Physical Setup

6.1.1 Optical Setup

An annotated image of the physical optical setup can be seen in figure 6.1. A close-up annotated image of the chip can be seen in figure 6.2.

6.1.2 Other Components

Other components of the experiment include a broadband SuperK laser, an HMP4040 power source and a spectrometer with a PIXIS 1024 camera. The SuperK laser is connected through fibers to the optical setup, and the output from the optical setup is again carried by the fibers to the spectrometer. HMP4040 is used as the voltage source when performing actuation measurements.

6.2 Codebase for GUI and Automation

All the codebase for GUI and automation is written in Python due to its flexibility and several package offerings for easy communication between devices. An overview can be seen in figure 6.3.

A sample image from the GUI can be seen in figure 6.4. The GUI is used for making it easier to interact with the various experimental instruments, obtain and save data. It is also used to input various parameters required for automated signal optimization and device characterization, the state diagram of which can be seen in figure 6.5.

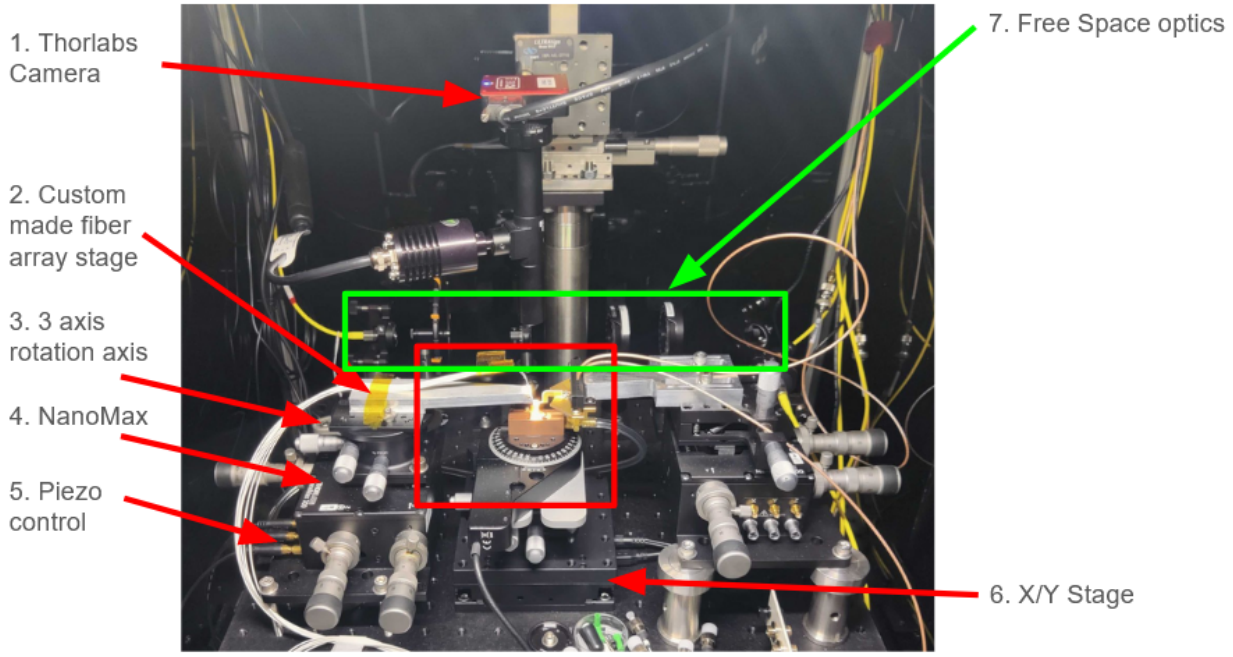

Figure 6.1: An annotated image of the optical setup. Key components are highlighted. Free space optics is used for adjusting OD and polarization of the laser. Zoomed-in version of the red square (i.e. the chip setup) can be seen in 6.2. Image taken from [19].

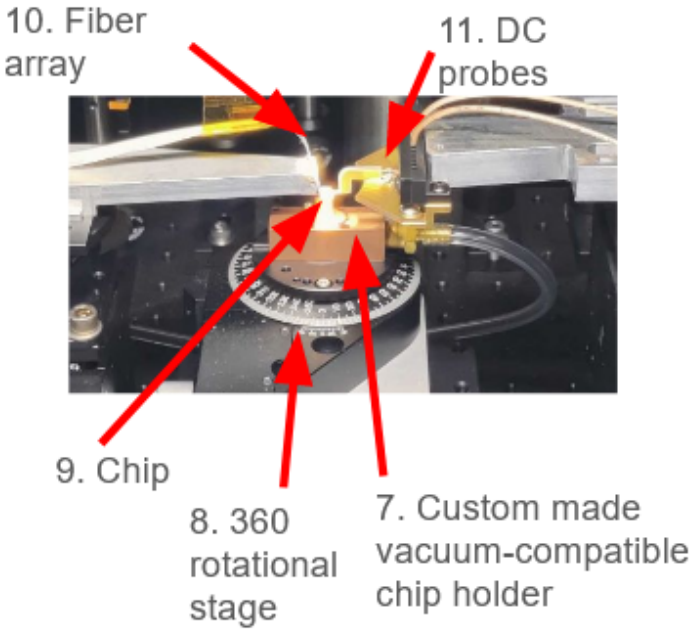

Figure 6.2: Zoomed-in chip setup. The fiber array can be seen to make 18° with the vertical, as this is the optimum angle for used wavelengths. DC probes are used for MEMS actuation, and the vacuum-compatible chip holder is to ensure the chip does not slide. Image taken from [19].

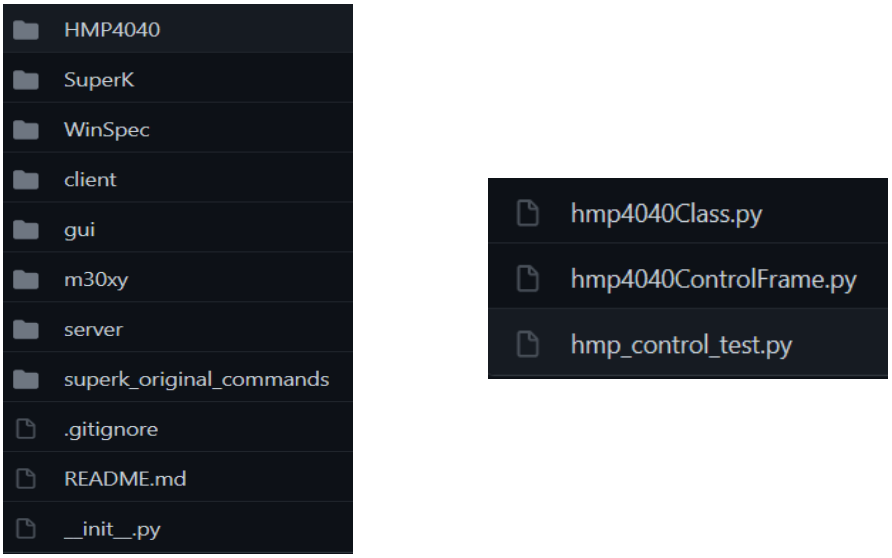

Figure 6.3: An overview of the codebase. Each parent folder (left) contains the GUI and control code for a specific instrument, along with some occasional test code and old code (right). The GUI is started by running "`gui/gui_run.py`".

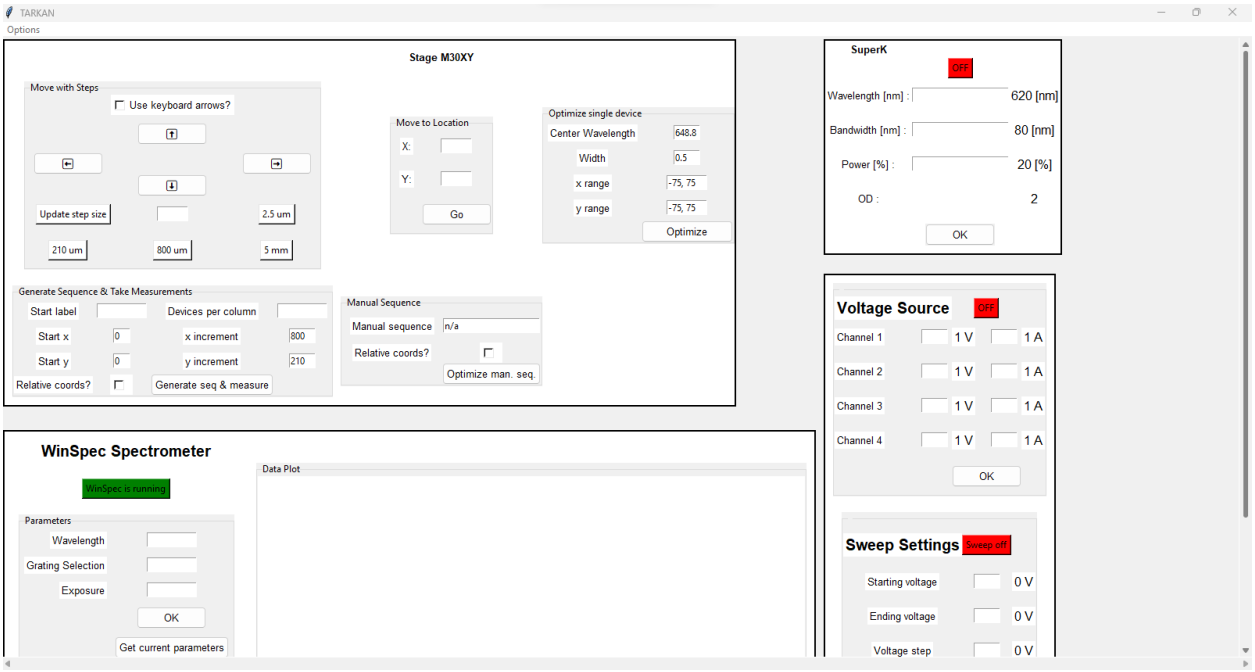

Figure 6.4: A sample image from the GUI. There are different tabs that the user can activate for interacting with different piece of equipment. The user can input starting device coordinates, wavelength of interest, voltage range and step size along with some other parameters to start an "automated sweep." Starting from the input device coordinates, the algorithm first finds the optimal location of the fiber array for the output signal in the spectrometer, then saves spectral measurements for different voltages at the optimal location, and finally proceeds to the next device. These steps are repeated until the last specified location on the chip is reached. There is also a frame (bottom left) to plot live data from the spectrometer.

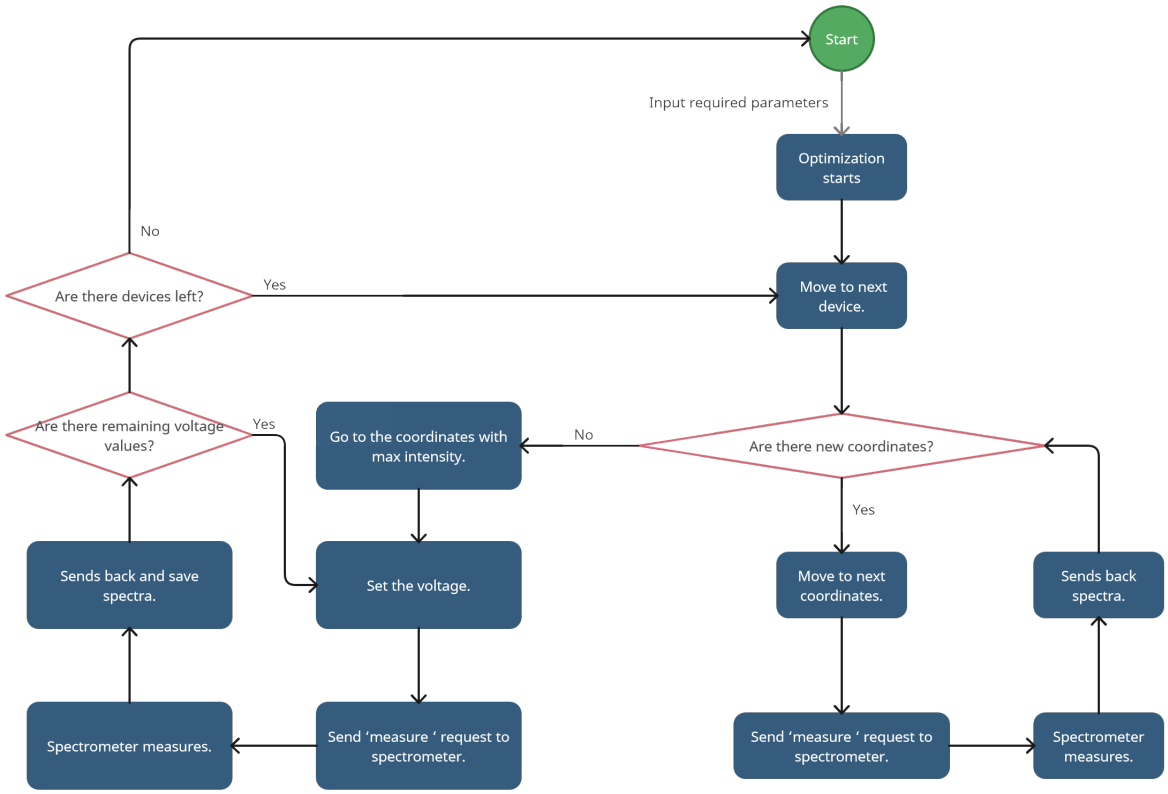

Figure 6.5: A simplified state machine for the automated device characterization. Some of the important parameters required for automation are mentioned in figure 6.4.

Chapter 7

Loss Analysis for Waveguides at 647 nm

In this chapter, we will shift gears and talk about the experimental results that we have got so far, comparing with the theory.

As will be explained in chapter 8, there weren't any active MZI measurements due to MEMS actuation failure. However, using the test structures on the chip, we were able to characterize the two important sources of losses for these waveguides: bending and propagation losses.

In general, there is no reason to expect that the waveguide loss will be the same for all the wavelengths. In theory, one should perform this loss characterization for every wavelength of concern. In our experiments, we characterized the loss for the SiN waveguides for 647 nm. The choice of 647 nm was rather arbitrary, with the only requirement being that the chosen wavelength must be close to the design wavelength of the waveguides, 620 nm. Our main goal was to understand the general trend that the loss follows as a function of the number of 90° turns in the waveguide and the propagation length.

Both the bending and the propagation losses were measured using the 4 bending and spiral waveguides available on the chip, shown in figures 4.7) and **??** respectively.

The total number of 90° circles and approximate waveguide lengths for the measured bending waveguides can be seen in table 7.1. All the quarter-circles had an approximate radius of $R_1 = 10.0\,\mu m$, and the length of the straight portion of the waveguide connecting two quarter-circles was approximately $L_1 = 3.92\,\mu m$. Hence, the approximate waveguide lengths were calculated using the formula length = (number of turns) $\times \frac{\pi}{2} R_1 +$ (number of turns) $\times\, l$.

The total number of 90° circles and approximate waveguide lengths for the spiral waveguides can be seen in table 7.2. All the quarter-circles were approximated to have a mean radius of $R_2 = 11.7\,\mu m$ for calculation purposes. However, from the GDS file, it seems that each quarter-circle has a slightly different radius, which probably is one of the main contributors to the deviation of the theoretical model from measurements, as will be explained later in this chapter.

We give each waveguide a number for easier referring.

The measured intensities at the spectrometer can be seen at tables 7.3 and 7.4 along with the OD values used for measurements and normalization of intensities. For all the measurements, the reference intensity used was the intensity at 647 nm with OD = 6: $I_{ref} = 6059 \times 10^6$. Each measurement was repeated 4 times.

The measured losses converted to dB plotted with the standard deviations can be seen in

Number	Number of 90° circles	Waveguide length (μm)	Length of straight portion (μm)
1	22	432	86
2	54	1060	212
3	104	2041	407
4	198	3886	776

Table 7.1: The properties of the bending waveguides.

Number	Number of 90° circles	Waveguide length (μm)	Length of straight portion (μm)
5	21	1355	969
6	28	2043	1528
7	52	4817	3861
8	100	13333	11495

Table 7.2: The properties of the spiral waveguides.

Number	Average measured intensity (a.u.)	OD
1	52437.25	2
2	34544.25	2
4	15885.0	2
4	5486.0	2

Table 7.3: Bending waveguide loss measurements with the OD used.

Number	Average measured intensity (a.u.)	OD
5	44260.0	2
6	32034.0	2
7	11682.5	2
8	16203.25	0.5

Table 7.4: Spiral waveguide loss measurements with the OD used.

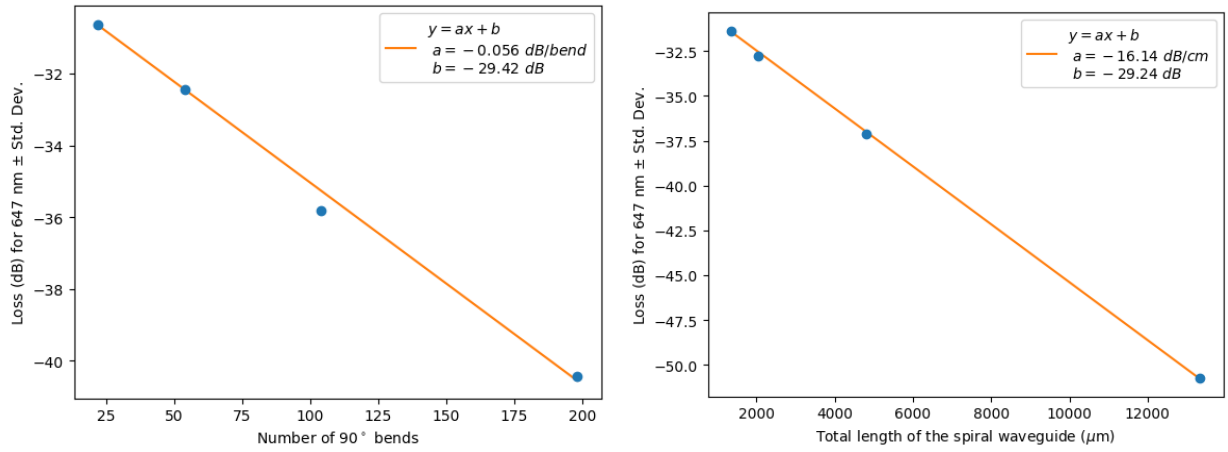

Figure 7.1: The dB losses for 647 nm for the bending waveguides on the left, and the spiral waveguides on the right. As can be seen, the dB loss is linearly increasing with the number of bends and distance travelled. The standard deviations are plotted as the error bars but are too tiny to be visible.

figure 7.1. We can see the extracted values of $dB/bend$ and dB/cm on the figures. We can now use these values to extract the α and β loss coefficients defined in eq. 3.24. Since the straight portions of the bending waveguide constitute around 19.5% of the entire waveguide, the losses in straight portions can not be neglected (see table 7.1). Likewise, the bending portions of the spiral waveguides forms at least 13.7% of the entire waveguide, therefore the bending losses have to be accounted for as well. To account for these losses, we write the following equation for a bending waveguide with N turns, using eq. 3.24 and the parameters of the dB line from figure 7.1:

$$I_{\text{measured}} = I_{\text{input}} \left(e^{-\beta \frac{\pi R_1}{2}} e^{-\alpha L_1} \right)^N = I_{\text{input}} \left(e^{-N\left(\beta \frac{\pi R_1}{2} + \alpha L_1\right)} \right) = I_{\text{input}} 10^{\frac{a_{\text{bend}} N}{10}} \tag{7.1}$$

$$\Rightarrow \beta \frac{\pi R_1}{2} + \alpha L_1 = -\frac{a_{\text{bend}}}{10} \ln 10 \tag{7.2}$$

where L_1 is the straight waveguide segment that comes after each bend, $I_{input} = I_0 10^{\frac{b_{\text{bend}}}{10}}$ is the intensity input to the chip surface, and $a_{\text{bend}} = -0.056\ dB/bend$. At each bend, the intensity decreases by a factor of $e^{-\beta \frac{\pi R_1}{2}} e^{-\alpha L_1}$, hence after N such bends we measure the above intensity.

Similarly, we can write the following equation for the spiral waveguides:

$$I_{\text{measured}} = I_{\text{input}} e^{-\beta \frac{\pi R_2}{2} N} e^{-\alpha\left(L_2 - \frac{\pi R_2}{2} N\right)} = I_{\text{input}} 10^{\frac{a_{\text{spiral}} L_2}{10}} \tag{7.3}$$

$$e^{-\beta \frac{\pi R_2}{2} N} e^{-\alpha\left(L_2 - \frac{\pi R_2}{2} N\right)} = 10^{\frac{a_{\text{spiral}} L_2}{10}} \tag{7.4}$$

where $L_2 - \frac{\pi R_2}{2} N$ is the total length of the straight portion of the waveguide with L_2 being the total length, and $I_{input} = I_0 10^{\frac{b_{\text{spiral}}}{10}}$ is the intensity input to the chip surface, and $a_{\text{spiral}} = -16.14\ db/cm$.

Finally, we can use eqs. 7.2 and 7.4 to calculate the unknown α and β. The first eq. does not depend on N or the total length of the waveguide, while the second depends on N and also the total length L_2. Thus, we will pick the first data point in table 7.2, calculate α and β, and compare compare how well this model predicts the the losses for the other data points. Doing so results in

$$\begin{cases} \alpha = 2.04\ dB/cm \\ \beta = 7.82\ dB/cm \end{cases}$$

As we expect, the loss coefficient in the bend is higher than the straight portion, as propagation losses contribute to but are not the only sources of losses in the bend. We also note that the value for α is similar to other measurements done for SiN waveguides in the literature (Please see [20]. Although this work measured the propagation loss at 1550 nm, we see that the order of magnitude of our measured propagation loss matches with the reported value of 2.1 dB/cm in that work.).

The loss factor (the exponential factor from eqs. 7.1 and 7.3) predictions from this model and the dB curve fit can be seen in table 7.5. The line fits well to the measured intensities, so we will just use the y values of the fit as the measured loss factor.

Number	Predicted loss factor	Measured loss factor
1	0.750	0.753
2	0.493	0.498
3	0.257	0.262
4	0.0750	0.0778
5	0.607	0.607
6	0.490	0.471
7	0.215	0.170
8	0.0228	0.00736

Table 7.5: Loss factor comparison for the predicted and the measured factors. There is generally quite good agreement between the model and the experiment for the bending waveguides (1-4). But it should be noted that for the spiral waveguide, as the total length increases, the discrepancy between the model and the experiment increases. This suggests this model is either not so good at describing the losses at waveguides that are more than 80% straight, or there were some measurement errors from the GDS file, or the assumption that the variation in β can be neglected is wrong.

Even though there are discrepancies between the model and the experiment for longer spiral waveguides, the model can predict the loss factors in bending waveguides with errors as little as 3.6%. Thus, this simple model assuming two different exponential decay coefficients for the straight and bent waveguides seems to capture the loss properties for shorter ($<\sim$ 4000 µm) and bent-heavy (more than 80%) waveguides up to errors of 3.6%.

Chapter 8

Current Experimental Problems and Future Directions

As closing remarks, we will briefly touch on the current experimental problems and future directions. There are two main problems with MEMS characterization as of writing this thesis: 1) The collapse of the cantilever, 2) Etching of the metal pads used for voltage application.

We have observed that there were several MEMS devices with collapsed cantilevers straight out of fabrication. We tried to place the chip on a probe station, and "poke" the cantilevers gently until they were released. This resulted in some of the waveguides being broken. Nevertheless, we were able to visually confirm that some of the collapsed cantilevers were released, because we could either see the shadow under the cantilever under light microscope, or we could see the probe tips getting in between the cantilever and the fixed waveguide, or we could see the cantilever "snap free" when poked with the probes. However, despite confirming some of the devices were not collapsed, we were still not able to observe the expected phase shifts.

After observing no displacements in cantilever arms despite going as high as 120 V, we eventually suspected there could be faulty electrical connections on the chip. There were some electrical test structures on the chip, consisting of pads directly connected to each other. We tested connectivity between these pads and saw that almost all of them showed resistance orders of magnitude higher than what would be expected from two electrically connected conductors. We then looked at electrical pads specifically under microscope and saw traces of corrosion. Our hypothesis is that the etching processes etched the electrical pads and other metal connections on the chip surface, thus preventing us from actuating devices.

In the future, we would first like to improve the fabrication process to not etch away the metal pads and connectors on the chip, and second, develop a more reliable method of preventing cantilever collapse, or releasing them.

References

[1] C. Errando-Herranz, A. Y. Takabayashi, P. Edinger, H. Sattari, K. B. Gylfason, and N. Quack, "Mems for photonic integrated circuits," *IEEE Journal of Selected Topics in Quantum Electronics*, vol. 26, no. 2, Apr. 2020.

[2] S. Rumley, "Silicon photonics for exascale systems," *J. Lightw. Technol.*, vol. 33, no. 3, Feb. 2020.

[3] J. W. Silverstone, D. Bonneau, J. L. O'Brien, and M. G. Thompson, "Silicon quantum photonics," *IEEE J. Sel. Topics Quantum Electron*, vol. 22, no. 6, Nov. 2016.

[4] E. Homepage. "Europractice homepage." (May 2024), URL: https://europractice-ic.com/.

[5] MOSIS. "Mosis." (May 2024), URL: https://themosisservice.com/.

[6] S. T. Lim, M. J. Sun, and C. E. Png, "Silicon optical modulator simulation," *Front. Phys.*, vol. 3, Apr. 2015.

[7] Wikipedia. "Pockels effect." (2024), URL: https://en.wikipedia.org/wiki/Pockels_effect.

[8] Nanohub. "History of mems." (2017), URL: https://nanohub.org/resources/26535/download/App_Intro_PK10_PG.pdf.

[9] Z. Han, P. Zhang, and S. I. Bozhevolnyi, "Calculation of bending losses for highly confined modes of optical waveguides with transformation optics," *Optics Letters*, vol. 38, 2013.

[10] Synopsys. "Computing bending modes." (2024), URL: https://www.synopsys.com/photonic-solutions/product-applications/waveguides-and-fibers/bending-modes.html.

[11] FOSCO. "Optical waveguide field equations." (2024), URL: https://www.fiberoptics4sale.com/blogs/wave-optics/field-equations.

[12] FOSCO. "Wave equations for optical waveguides." (2024), URL: https://www.fiberoptics4sale.com/blogs/wave-optics/wave-equations-for-optical-waveguides.

[13] G. P. Agrawal, *Applications of Nonlinear Fiber Optics*, 3rd ed. Academic Press, 2020.

[14] W. Huang, "Coupled-mode theory for optical waveguides: An overview," *Journal of the Optical Society of America*, vol. 1, 1994.

[15] M. Yucel, "Photonic integrated circuits for large-scale quantum information processing with artificial atoms," Master's Thesis, MIT, 2022.

[16] S. Schmid, C. Hierold, and A. Boisen, "Modeling the kelvin polarization force actuation of micro- and nanomechanical systems," *Journal of Applied Physics*, vol. 107, 2010.

[17] L. Cheng, S. Mao, Z. Li, Y. Han, and H. Fu, "Grating couplers on silicon photonics: Design principles, emerging trends and practical issues," *Micromachines*, Jul. 2020.

[18] C. Multiphysucs. "Comsol." (2024), URL: www.comsol.com.

[19] M. Yucel, *Optical setup presentation*, Online presentation, Dec. 2023.

[20] S. C. Mao, S. H. Tao, Y. L. Zu, X. W. Sun, M. B. Yu, and G. Q. L. an dD. L. Kwong, "Low propagation loss sin optical waveguide prepared by optimal low-hydrogen module," *Optics Letters*, vol. 16, 2008.